

© 2019 by Akshat Puri. All rights reserved.

MEASUREMENT OF ANGULAR AND MOMENTUM DISTRIBUTIONS OF CHARGED
PARTICLES WITHIN AND AROUND JETS IN Pb+Pb AND $p\bar{p}$ COLLISIONS AT
 $\sqrt{S_{NN}} = 5.02$ TeV WITH ATLAS AT THE LHC

BY
AKSHAT PURI

DISSERTATION

Submitted in partial fulfillment of the requirements
for the degree of Doctor of Philosophy in Physics
in the Graduate College of the
University of Illinois at Urbana-Champaign, 2019

Urbana, Illinois

Doctoral Committee:

Professor Matthias Grosse Perdekamp, Chair
Professor Anne Marie Sickles, Advisor
¹ Professor Aida El-Khadra
Professor Bryce Gadaway

Abstract

² Studies of the fragmentation of jets into charged particles in heavy-ion collisions can help in understanding
³ the mechanism of jet quenching by the hot and dense matter created in such collisions, the quark-gluon
⁴ plasma. This thesis presents a measurement of the angular distribution of charged particles around the jet
⁵ axis as measured in Pb+Pb and pp collisions collided at a center of mass energy of $\sqrt{s_{NN}} = 5.02$ TeV. The
⁶ measurement is done using the ATLAS detector at the Large Hadron Collider, and utilizes 0.49 pb^{-1} of
⁷ Pb+Pb and 25 pb^{-1} of pp data collected in 2015. The measurement is performed for jets reconstructed
⁸ with the anti- k_t algorithm with radius parameter $R = 0.4$, and is extended to regions outside the jet cone.
⁹ Results are presented as a function of Pb+Pb collision centrality, and both jet and charged-particle transverse
¹⁰ momenta. It was observed that in Pb+Pb collisions there is a broadening of the jet for charged particles with
¹¹ $p_T < 4$ GeV, along with a narrowing for charged particles with $p_T > 4$ GeV. Ratios between the angular
¹² distributions in Pb+Pb and pp showed an enhancement for particles with $p_T < 4$ GeV in Pb+Pb collisions,
¹³ with the enhancement increasing up to 2 for $r < 0.3$, and remaining constant for $0.3 < r < 0.6$. Charged
¹⁴ particles with $p_T > 4$ GeV show a small enhancement in the jet core for $r < 0.05$, with a growing suppression
¹⁵ of up to 0.5 for $r < 0.3$ in Pb+Pb collisions. The depletion remains constant for $0.3 < r < 0.6$.

For my Mother, Father, and Brother

Contents

| | | |
|---------------|---|----------|
| ¹⁸ | Chapter 1 Theoretical Introduction | 1 |
| ¹⁹ | 1.1 Quantum Chromodynamics | 1 |
| ²⁰ | 1.2 Heavy Ion Collisions and the Quark Gluon Plasma | 4 |
| ²¹ | 1.2.1 Heavy Ion Collisions | 4 |
| ²² | 1.2.2 The Quark Gluon Plasma | 6 |
| ²³ | 1.3 Jets and Jet Quenching | 7 |

Chapter 1

Theoretical Introduction

This section shall discuss the theoretical background necessary to understand jet measurements. It will discuss the fundamentals of quantum chromodynamics (QCD), the heavy ion collision system and the quark gluon plasma that is formed, and finally jets and jet energy loss.

1.1 Quantum Chromodynamics

Quantum Chromodynamics is a gauge theory with SU(3) symmetry that describes the dynamics of the strong interactions between quarks and gluons. It is part of the Standard Model [1], the building blocks of which are shown in Figure 1.1.

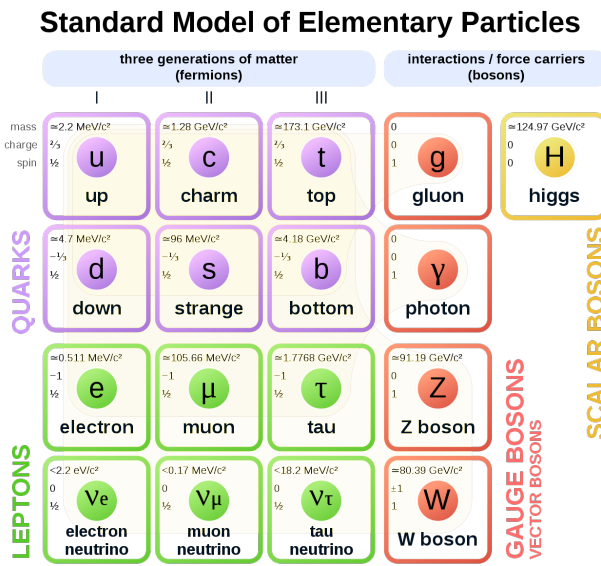


Figure 1.1: The elementary particles of the standard model.

Quarks are fermions with a spin of 1/2, and carry a fractional electric charge as well as a color charge. They all have mass and come in six flavors: up, down, top, bottom, strange, charm. The lightest quarks

³⁴ (u and d) combine and form stable particles, while the heavier quarks can only be produced in energetic
³⁵ environments and decay rapidly. Gluons are gauge bosons (force carriers) with a spin of 1, and are what hold
³⁶ quarks together. The dynamics of the quarks and gluons are described by the QCD Lagrangian given as [2]:

$$\mathcal{L}_{\text{QCD}} = \sum_q \bar{\psi}_{q,a} (i\gamma^\mu \partial_\mu \delta_{ab} - g_s \gamma^\mu t_{ab}^C \mathcal{A}_\mu^C - m_q \delta_{ab}) \psi_{q,b} - \frac{1}{4} F_{\mu\nu}^A F^{A\mu\nu} \quad (1.1)$$

³⁷ where $\psi_{q,a}$ and $\psi_{q,b}$ are quark-filled spinors for a quarks with flavor q , mass m_q , and color a and b respectively,
³⁸ with the values for a and b ranging from 1 to 3 (for the three colors). The \mathcal{A}_μ^C corresponds to the gluon field
³⁹ with C taking values from 1 through 8 (for the 8 types of gluons). The t_{ab}^C corresponds to the Gell-Mann
⁴⁰ matrices that are the generators of the SU(3) group, and dictate the rotation of the quarks color in SU(3)
⁴¹ space when it interacts with a gluon. The coupling constant is encoded within g_s , which is defined by
⁴² $g_s \equiv \sqrt{4\pi\alpha_s}$. The field tensor $F_{\mu\nu}^A$ can be written in terms of the structure constants of the SU(3) group
⁴³ f_{ABC} , and is given by:

$$F_{\mu\nu}^A = \partial_\mu \mathcal{A}_\nu^A - \partial_\nu \mathcal{A}_\mu^A - g_s f_{ABC} \mathcal{A}^B \mathcal{A}^C \quad (1.2)$$

⁴⁴ While many parallels can be drawn between Quantum Electrodynamics (QED, the theory that describes
⁴⁵ photons and electrons) and QCD, the difference between the two comes from the gluon-gluon interactions
⁴⁶ allowed in QCD, making it non-Abelian. These interactions can be summarized as shown in Figure 1.2.

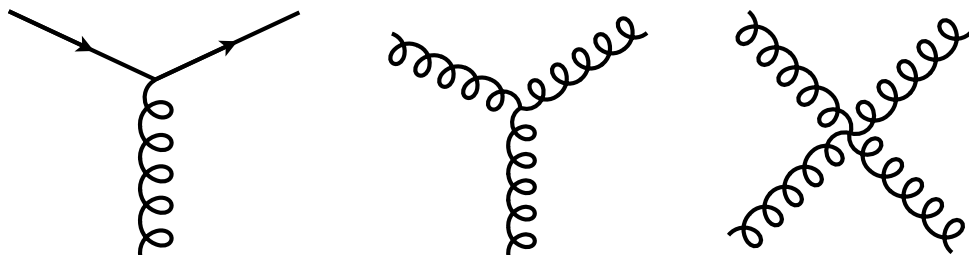


Figure 1.2: The allowed vertices in QCD. The vertices involving two or more gluons are unique to QCD and do not have a QED analog.

⁴⁷ A core feature of QCD is that the coupling constant α_s has an energy dependence shown in Figure 1.3.
⁴⁸ This dependence can be expressed in terms of the β function as

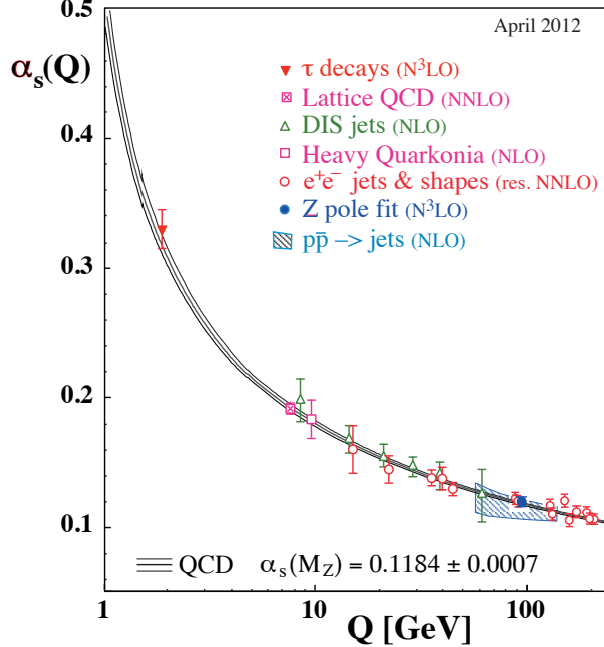


Figure 1.3: The running coupling constant α_s as a function of the momentum transfer Q . Figure taken from Ref. [2].

$$Q^2 \frac{\partial \alpha_s(Q^2)}{\partial Q^2} = \beta(\alpha_s(Q^2)) \quad (1.3)$$

49 where Q is the momentum transfer in the particle reaction. The beta function can be expressed using
50 perturbative QCD (pQCD) as

$$\beta(\alpha_s) = -(b_0 \alpha_s^2 + b_1 \alpha_s^3 + b_2 \alpha_s^4 \dots) \quad (1.4)$$

51 where the coefficients b_i depend on the number of colors and flavors.

52 This running coupling constant is small and asymptotically tends to zero at large energy scales (or at
53 small distances) and is large at small energy scales (large distances). This running coupling phenomenon
54 leads to two key behaviors: asymptotic freedom and color confinement.

55 **Asymptotic Freedom:** At high energy scales (small distances), the QCD coupling constant α_s is
56 small and tends to zero, implying a free particle behavior of quarks and gluons. This has been observed by a

57 variety of deep inelastic experiments [3–16]

58 **Color Confinement** The opposite end of the running coupling constant phenomenon is color confinement.
59 This property of QCD forbids the direct observation of free quarks and gluons, allowing only for
60 composite particles that are color singlets.

61 1.2 Heavy Ion Collisions and the Quark Gluon Plasma

62 Heavy ion collisions were suggested in Reference [17] as a tool to study the Quark Gluon Plasma. They
63 provide access to the otherwise confined partons, and give insight into the QCD phase diagram and the
64 transition between the QGP and hadronic matter. This section will briefly discuss a heavy ion collision and
65 the properties of the medium that is formed in such a collision.

66 1.2.1 Heavy Ion Collisions

67 In a heavy ion collision, the colliding nuclei are Lorentz contracted discs. In the case of a Pb+Pb collision,
68 the nuclei have been accelerated to energies where the relativistic γ factor is between 100 and 2500 for
69 beam rapidities of $y = 5.3$ and 8.5 . Each nucleus contains many colored quarks and antiquarks, with three
70 more quarks than anti-quarks per nucleon, with the $q\bar{q}$ popping in and out of the vacuum due to quantum
71 fluctuations. These $q\bar{q}$ pairs are sources of transverse color fields and the corresponding force carriers, the
72 gluons.

73 When these pancake like discs collide, their color fields interact and there is a color charge exchange,
74 producing longitudinal color fields that fill the space between the receding discs. While the maximum energy
75 density in the process occurs just at the collision, the energy density 1 fm/c after the collision is 12 GeV/fm^3 ,
76 much higher than the 500 MeV/fm^3 in a typical hadron. Lattice QCD calculations in thermodynamics show
77 that at these energies, the partons produced in the collision cannot be treated as a collection of distinct
78 hadrons. In fact, these partons are strongly coupled to each other and form a medium called the Quark
79 Gluon Plasma (QGP) [??].

80 After the collision the energy density between the receding nuclei starts to decrease as the QGP cools and
81 expands. This process, seen in Figure 1.6, continues till the energy density drops to below that within a
82 hadron and the fluid “hadronizes”. These individual hadrons briefly scatter off of each other before they
83 freely fly towards the detector (freeze-out).

84 While Figure 1.6 shows snapshots of a head on (central) collision between two large nuclei, it is possible to
85 have collisions where the impact parameter is larger and hence the overlap region is smaller. These collisions,

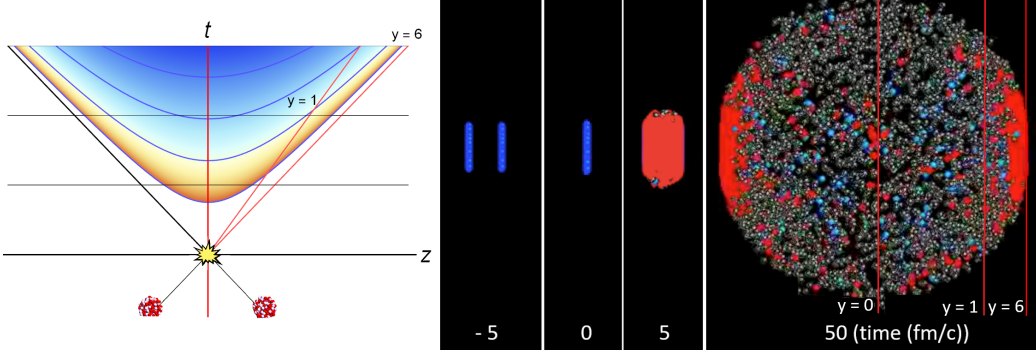


Figure 1.4: (left) Space-time diagram for a heavy ion collision. The color is indicative of the temperature of the QGP formed. (right) Snapshots of a heavy ion collision at $\sqrt{s_{NN}} = 2.76$ TeV at different times. The Lorentz contracted nuclei are in blue while the QGP is in red. Figures from References [7, 8].

86 called peripheral collisions, qualitatively undergo the same process described above, with the size and shape
87 of the QGP being different.

88 Basic parameters of a heavy ion collision such as the number of participants N_{part} and number of binary
89 collisions N_{coll} can be determined using the Glauber Monte Carlo simulations [18]. This technique considers
90 multiple scatterings of nucleons in nuclear targets by modeling the nucleus as a set of uncorrelated nucleons
91 sampled from measured density distributions. Two nuclei are arranged with a random impact parameter and
92 projected onto the $x - y$ plane as shown in Figure ??, with interaction probabilities being applied by using
93 the relative distance between nucleon centroids as a proxy for the measured inelastic nucleon-nucleon cross
94 section.

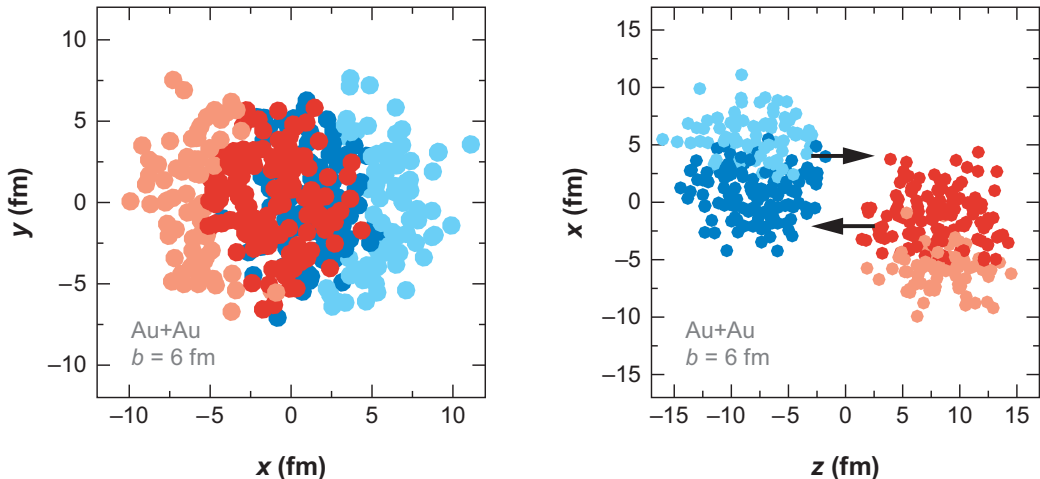


Figure 1.5: A Glauber Monte Carlo event for $Au + Au$ at $\sqrt{s_{NN}} = 200$ GeV with impact parameter of 6 fm viewed in the (left) transverse plane and (right) along the beam axis. Darker circles represent the participating nucleons. Taken from [18].

1.2.2 The Quark Gluon Plasma

Quarks and gluons are deconfined at extremely high energy and density conditions and form a state called the Quark Gluon Plasma [17]. These conditions are met in high energy heavy ion collisions. The Quark Gluon Plasma has to be described in terms of its constituent quarks and gluons as opposed to the hadrons. This transition between confinement within hadrons and being free within the QGP occurs at very high temperatures and pressures. This can be seen in the QCD phase diagram shown in Figure ??.

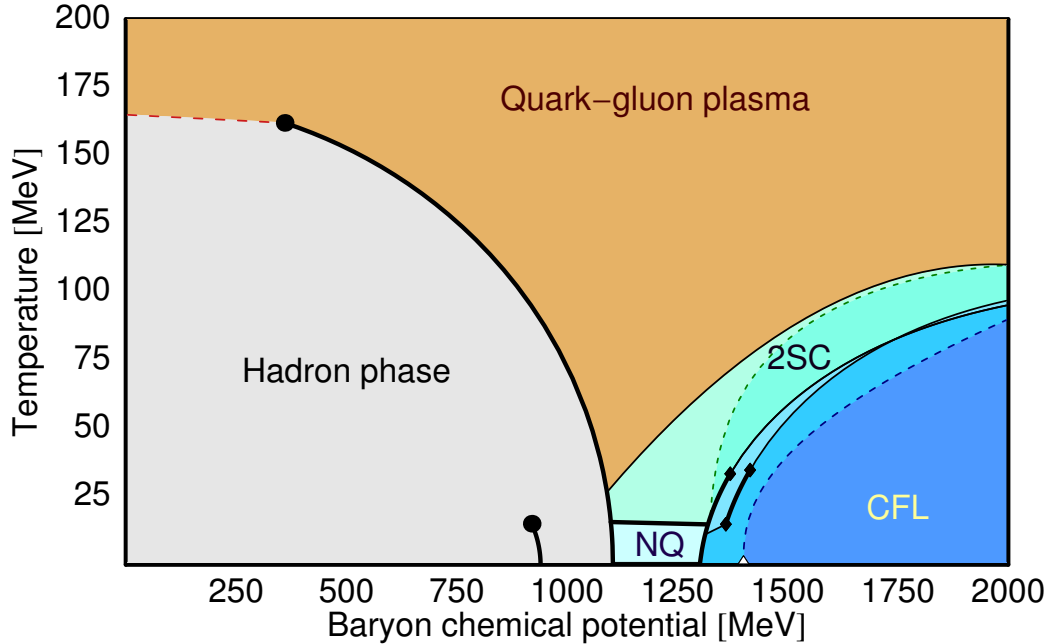


Figure 1.6: The QCD phase diagram of nuclear matter. Figure from Reference [19].

This state of matter exists above $\lambda_{\text{QCD}} = 200 \text{ MeV}$, the fundamental energy scale in QCD, and is believed to have filled the early universe a few microseconds after the Big Bang [23, 24] and might be present in the cores of extremely compact objects like neutron stars.

The MIT Bag Model can be used to describe the QGP as a simple ideal gas with a bag constant B that parameterizes the vacuum pressure [20, 21].

The QGP was initially thought to be a weakly coupled parton gas. This was based on asymptotic freedom from QCD; the highly energetic collisions such as those at the LHC would imply a weak interaction between the quarks and gluons that make up the plasma. This would result in rare scatterings between the constituents of the gas and wash out any spatial anisotropies based on the collision geometry. On the other hand, if the QGP is assumed to be strongly coupled, the pressure gradients in the medium would be driven by hydrodynamics and transform spatial anisotropies to momentum anisotropies in the particles

112 produced as shown in Figure 1.7. In this picture, the non-uniform structure of the colliding nuclei would
 113 cause a momentum anisotropy that would be further enhanced when looking at collisions that are less central
 114 and do not have perfect overlap between the colliding nuclei [116, 117, 118, 63]. Azimuthal correlation
 115 measurements [22–27] indicate momentum anisotropy in the collision, implying that the medium is strongly
 116 coupled.

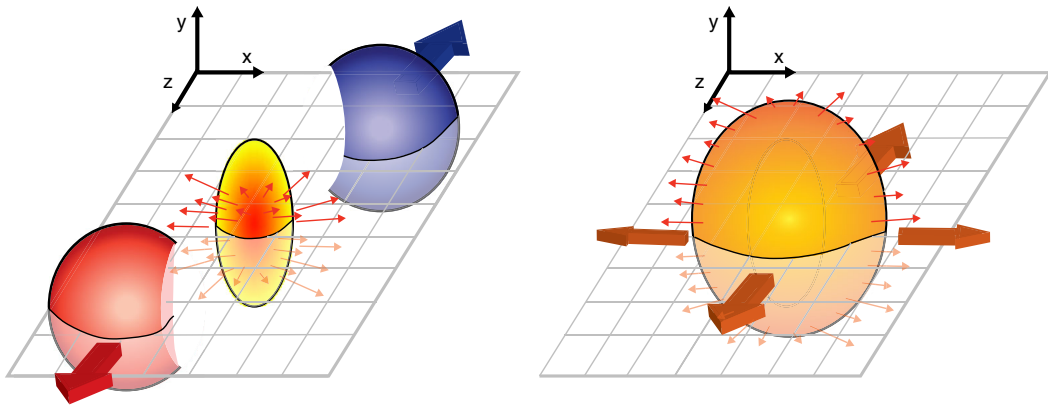


Figure 1.7: Schematic diagrams of the initial overlap region (left) and the final spatial anisotropy generated (right). Taken from [28].

117 A Fourier Transform of the angular distribution of charged hadrons in the collision debris can quantify
 118 these momentum anisotropies and give the anisotropic flow coefficients v_n , defined as [115]:

$$\frac{d\bar{N}}{d\phi} = \frac{\bar{N}}{2\pi} \left(1 + 2 \sum_{n=1}^{\inf} v_n \cos(n(\phi - \bar{\Psi}_n)) \right) \quad (1.5)$$

119 where ϕ is the angle in the transverse plane, $\bar{\Psi}_n$ are the event plane angles, and \bar{N} is the average number
 120 of particles per event. Some of these coefficients are shown in Figure 1.8.

121 Thermal photons from the QGP reveal that it reaches temperatures of 300–600 MeV in central collisions
 122 at 200 GeV [29] and 2.76 TeV [30], showing very little collision energy dependence. Further, the chemical
 123 freeze-out temperature was found to be 160 MeV via measurements of ratios of final state hadrons [31–33]
 124 with the thermal freeze-out being 100–150 MeV [34–37].

125 1.3 Jets and Jet Quenching

126 Hard scatterings in the colliding nuclei result in the production of highly energetic partons that evolve, decay,
 127 and eventually form conical sprays of particles called jets. Jet production is well understood in a pp collision

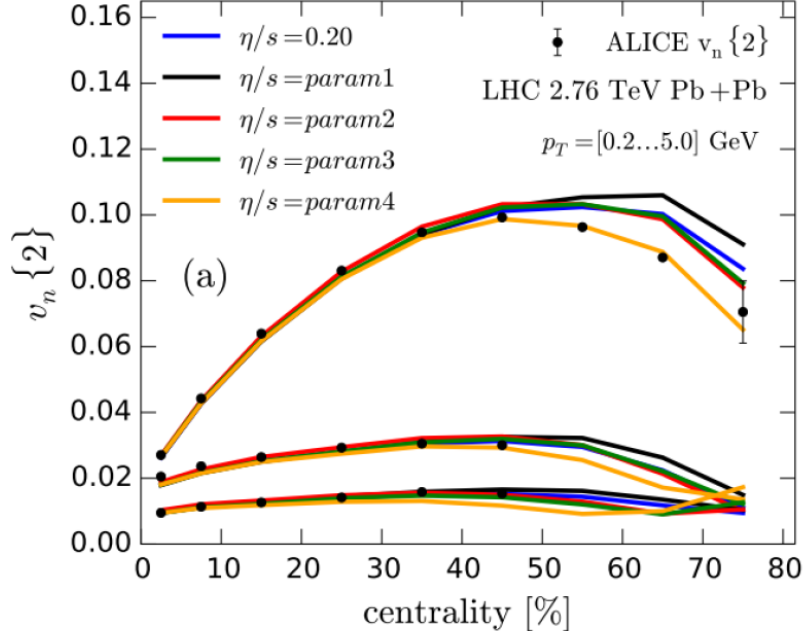


Figure 1.8: Comparison of a hydrodynamic model from [107] to the anisotropy measurements by ALICE [108] for different parameterizations of the η/s and for different $v_n(n = 2, 3, 4)$ from top to bottom as a function of collision centrality. – see ATLAS measurement from [109].

128 environment (where there are no QGP effects) in the context of perturbative QCD [161]. In heavy ion
 129 collisions, jets must traverse the quark gluon plasma. This can result in the jet losing energy and forward
 130 momentum [162, 163], while also picking up momentum transverse to the parton direction. Jets can also
 131 deposit energy in the medium, creating a wake [71, 70].

132 Jet production shown in Figure 1.9 can be written in terms of the parton distribution functions, scattering
 133 cross sections, and the fragmentation functions as

$$d\sigma_{pp \rightarrow hX} \approx \sum_{abjd} \int dx_a \int dx_b \int dz_j f_{a/p}(x_a, \mu_f) \times f_{b/p}(x_b, \mu_f) \quad (1.6)$$

$$\times d\sigma_{ab \rightarrow jd}(\mu_f, \mu_F, \mu_R) \quad (1.7)$$

$$\times D_{j \rightarrow h}(Z_j, \mu_f) \quad (1.8)$$

134 These are discussed in Section 1.3.

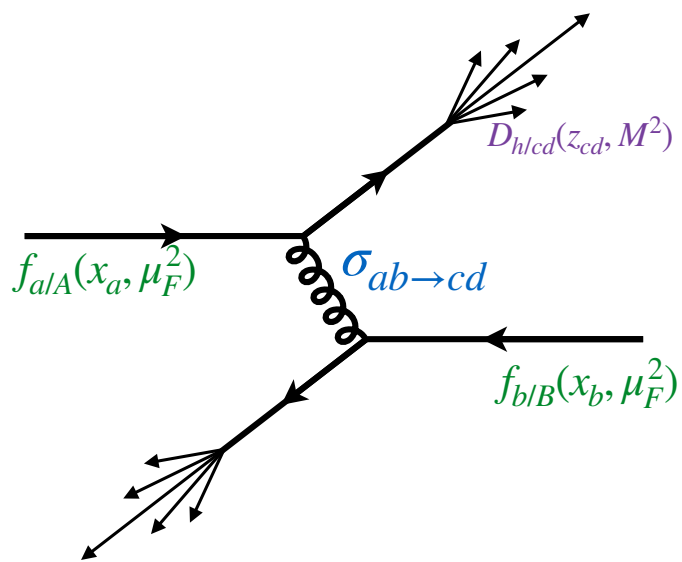


Figure 1.9: Jet production from the process $pp \rightarrow hX$, factorizing in terms of the parton distribution functions, scattering cross sections, and jet fragmentation functions. [[arXiv:1511.00790](https://arxiv.org/abs/1511.00790)]

Bibliography

- 135 [1] M. K. Gaillard, P. D. Grannis and F. J. Sciulli, *The Standard model of particle physics*, Rev. Mod.
136 Phys. **71** (1999) S96, arXiv: [hep-ph/9812285 \[hep-ph\]](#) (cit. on p. 1).
- 137 [2] J Beringer et al., *Review of Particle Physics, 2012-2013. Review of Particle Properties*, Phys. Rev. D
138 **86** (2012) 010001 (cit. on pp. 2, 3).
- 139 [3] A. Deur et al., *High precision determination of the Q^2 evolution of the Bjorken Sum*, Phys. Rev. D**90**
140 (2014) 012009, arXiv: [1405.7854 \[nucl-ex\]](#) (cit. on p. 4).
- 141 [4] J. H. Kim et al., *A Measurement of $\alpha_s(Q^2)$ from the Gross-Llewellyn Smith sum rule*, Phys. Rev. Lett.
142 **81** (1998) 3595, arXiv: [hep-ex/9808015 \[hep-ex\]](#) (cit. on p. 4).
- 143 [5] G. Altarelli et al., *Determination of the Bjorken sum and strong coupling from polarized structure
144 functions*, Nucl. Phys. **B496** (1997) 337, arXiv: [hep-ph/9701289 \[hep-ph\]](#) (cit. on p. 4).
- 145 [6] H. W. Kendall, *Deep inelastic scattering: Experiments on the proton and the observation of scaling*,
146 Rev. Mod. Phys. **63** (3 1991) 597 (cit. on p. 4).
- 147 [7] A. L. Kataev, G. Parente and A. V. Sidorov, *Improved fits to the xF_3 CCFR data at the next-to-next-to-
148 leading order and beyond*, Phys. Part. Nucl. **34** (2003) 20, [Erratum: Phys. Part. Nucl.38,no.6,827(2007)],
149 arXiv: [hep-ph/0106221 \[hep-ph\]](#) (cit. on p. 4).
- 150 [8] S. Alekhin, J. Blumlein and S. Moch, *Parton Distribution Functions and Benchmark Cross Sections at
151 NNLO*, Phys. Rev. D**86** (2012) 054009, arXiv: [1202.2281 \[hep-ph\]](#) (cit. on p. 4).
- 152 [9] S. Alekhin, J. Blumlein and S.-O. Moch, *ABM news and benchmarks*, PoS **DIS2013** (2013) 039, arXiv:
153 [1308.5166 \[hep-ph\]](#) (cit. on p. 4).
- 154 [10] J. Blumlein, H. Bottcher and A. Guffanti, *Non-singlet QCD analysis of deep inelastic world data at
155 $O(\alpha_s^3)$* , Nucl. Phys. **B774** (2007) 182, arXiv: [hep-ph/0607200 \[hep-ph\]](#) (cit. on p. 4).
- 156 [11] H1 Collaboration, *Three- and Four-jet Production at Low x at HERA*, Eur. Phys. J. **C54** (2008) 389,
157 arXiv: [0711.2606 \[hep-ex\]](#) (cit. on p. 4).

- 158 [12] ZEUS Collaboration, *Forward-jet production in deep inelastic ep scattering at HERA*, *Eur. Phys. J.*
 159 **C52** (2007) 515, arXiv: [0707.3093 \[hep-ex\]](https://arxiv.org/abs/0707.3093) (cit. on p. 4).
- 160 [13] ZEUS Collaboration, *Multi-jet cross-sections in charged current $e^\pm p$ scattering at HERA*, *Phys. Rev.*
 161 **D78** (2008) 032004, arXiv: [0802.3955 \[hep-ex\]](https://arxiv.org/abs/0802.3955) (cit. on p. 4).
- 162 [14] ZEUS Collaboration, *Inclusive dijet cross sections in neutral current deep inelastic scattering at HERA*,
 163 *Eur. Phys. J. C70* (2010) 965, arXiv: [1010.6167 \[hep-ex\]](https://arxiv.org/abs/1010.6167) (cit. on p. 4).
- 164 [15] ZEUS Collaboration, *Inclusive-jet cross sections in NC DIS at HERA and a comparison of the kT ,*
 165 *anti- kT and SIScone jet algorithms*, *Phys. Lett. B691* (2010) 127, arXiv: [1003.2923 \[hep-ex\]](https://arxiv.org/abs/1003.2923) (cit. on
 166 p. 4).
- 167 [16] H1 Collaboration, *Jet Production in ep Collisions at High Q^2 and Determination of α_s* , *Eur. Phys. J.*
 168 **C65** (2010) 363, arXiv: [0904.3870 \[hep-ex\]](https://arxiv.org/abs/0904.3870) (cit. on p. 4).
- 169 [17] E. V. Shuryak, *Quantum chromodynamics and the theory of superdense matter*, *Physics Reports*
 170 **61** (1980) 71 , ISSN: 0370-1573, URL: <http://www.sciencedirect.com/science/article/pii/0370157380901052> (cit. on pp. 4, 6).
- 172 [18] M. L. Miller, K. Reygers, S. J. Sanders and P. Steinberg, *Glauber Modeling in High-Energy Nuclear*
 173 *Collisions*, *Annual Review of Nuclear and Particle Science* **57** (2007) 205, eprint: <https://doi.org/10.1146/annurev.nucl.57.090506.123020>, URL: <https://doi.org/10.1146/annurev.nucl.57.090506.123020> (cit. on p. 5).
- 176 [19] S. B. Ruster, V. Werth, M. Buballa, I. A. Shovkovy and D. H. Rischke, *Phase diagram of neutral*
 177 *quark matter: Self-consistent treatment of quark masses*, *Phys. Rev. D* **72** (3 2005) 034004, URL:
 178 <https://link.aps.org/doi/10.1103/PhysRevD.72.034004> (cit. on p. 6).
- 179 [20] B. Müller, ‘Physics of the Quark-Gluon Plasma’, *Particle Production in Highly Excited Matter*, ed.
 180 by H. H. Gutbrod and J. Rafelski, Springer US, 1993 11, ISBN: 978-1-4615-2940-8, URL: https://doi.org/10.1007/978-1-4615-2940-8_2 (cit. on p. 6).
- 182 [21] K. Yagi, T. Hatsuda and Y. Miake, *Quark-gluon plasma: From big bang to little bang*, Camb. Monogr.
 183 Part. Phys. Nucl. Phys. Cosmol. **23** (2005) 1 (cit. on p. 6).
- 184 [22] ATLAS Collaboration, *Measurement of flow harmonics with multi-particle cumulants in Pb+Pb collisions*
 185 *at $\sqrt{s_{NN}} = 2.76$ TeV with the ATLAS detector*, *The European Physical Journal C* **74** (2014) 3157,
 186 ISSN: 1434-6052, URL: <https://doi.org/10.1140/epjc/s10052-014-3157-z> (cit. on p. 7).

- 187 [23] STAR Collaboration, *Identified Particle Elliptic Flow in Au + Au Collisions at $\sqrt{s_{NN}} = 130\text{GeV}$* , Phys.
 188 Rev. Lett. **87** (18 2001) 182301, URL: <https://link.aps.org/doi/10.1103/PhysRevLett.87.182301>
 189 (cit. on p. 7).
- 190 [24] PHENIX Collaboration, *Elliptic Flow of Identified Hadrons in Au+Au Collisions at $\sqrt{s_{NN}} = 200\text{ GeV}$* ,
 191 Phys. Rev. Lett. **91** (18 2003) 182301, URL: <https://link.aps.org/doi/10.1103/PhysRevLett.91.182301> (cit. on p. 7).
- 193 [25] PHOBOS Collaboration, *System Size, Energy, Pseudorapidity, and Centrality Dependence of Elliptic
 194 Flow*, Phys. Rev. Lett. **98** (24 2007) 242302, URL: <https://link.aps.org/doi/10.1103/PhysRevLett.98.242302> (cit. on p. 7).
- 196 [26] CMS Collaboration, *Measurement of higher-order harmonic azimuthal anisotropy in PbPb collisions at
 197 $\sqrt{s_{NN}} = 2.76\text{ TeV}$* , Phys. Rev. C **89** (4 2014) 044906, URL: <https://link.aps.org/doi/10.1103/PhysRevC.89.044906> (cit. on p. 7).
- 199 [27] ALICE Collaboration, *Anisotropic Flow of Charged Particles in Pb-Pb Collisions at $\sqrt{s_{NN}} = 5.02\text{ TeV}$* ,
 200 Phys. Rev. Lett. **116** (13 2016) 132302, URL: <https://link.aps.org/doi/10.1103/PhysRevLett.116.132302> (cit. on p. 7).
- 202 [28] M. Connors, C. Nattrass, R. Reed and S. Salur, *Jet measurements in heavy ion physics*, Rev. Mod. Phys.
 203 **90** (2 2018) 025005, URL: <https://link.aps.org/doi/10.1103/RevModPhys.90.025005> (cit. on
 204 p. 7).
- 205 [29] PHENIX Collaboration, *Enhanced Production of Direct Photons in Au + Au Collisions at $\sqrt{s_{NN}} =$
 206 200 GeV and Implications for the Initial Temperature*, Phys. Rev. Lett. **104** (13 2010) 132301, URL:
 207 <https://link.aps.org/doi/10.1103/PhysRevLett.104.132301> (cit. on p. 7).
- 208 [30] ALICE Collaboration, *Direct photon production in Pb–Pb collisions at $s_{NN}=2.76\text{ TeV}$* , Physics Letters
 209 B **754** (2016) 235 , ISSN: 0370-2693, URL: <http://www.sciencedirect.com/science/article/pii/S0370269316000320> (cit. on p. 7).
- 211 [31] Z. Fodor and S. Katz, *Critical point of QCD at finite T and λ , lattice results for physical quark
 212 masses*, Journal of High Energy Physics **2004** (2004) 050, URL: <https://doi.org/10.1088%2F1126-6708%2F2004%2F04%2F050> (cit. on p. 7).
- 214 [32] STAR Collaboration, *Experimental and theoretical challenges in the search for the quark–gluon plasma:
 215 The STAR Collaboration’s critical assessment of the evidence from RHIC collisions*, Nuclear Physics
 216 A **757** (2005) 102 , First Three Years of Operation of RHIC, ISSN: 0375-9474, URL: <http://www.sciencedirect.com/science/article/pii/S0375947405005294> (cit. on p. 7).

- 218 [33] ALICE Collaboration, *Production of light nuclei and anti-nuclei in pp and Pb-Pb collisions at energies*
219 *available at the CERN Large Hadron Collider*, Phys. Rev. C **93** (2 2016) 024917, URL: <https://link.aps.org/doi/10.1103/PhysRevC.93.024917> (cit. on p. 7).
- 220
221 [34] PHENIX Collaboration, *Single identified hadron spectra from $\sqrt{s_{NN}} = 130$ GeV Au + Au collisions*,
222 Phys. Rev. C **69** (2 2004) 024904, URL: <https://link.aps.org/doi/10.1103/PhysRevC.69.024904>
223 (cit. on p. 7).
- 224 [35] BRAHMS Collaboration, *Centrality dependent particle production at $y = 0$ and $y \geq 1$ in Au+Au collisions*
225 *at $\sqrt{s_{NN}} = 200$ GeV*, Phys. Rev. C **72** (1 2005) 014908, URL: <https://link.aps.org/doi/10.1103/PhysRevC.72.014908> (cit. on p. 7).
- 226
227 [36] PHOBOS Collaboration, *Identified hadron transverse momentum spectra in Au+Au collisions at*
228 *$\sqrt{s_{NN}} = 62.4$ GeV*, Phys. Rev. C **75** (2 2007) 024910, URL: <https://link.aps.org/doi/10.1103/PhysRevC.75.024910> (cit. on p. 7).
- 229
230 [37] ALICE Collaboration, *Centrality dependence of π , K , and p production in Pb-Pb collisions at $\sqrt{s_{NN}} =$
231 2.76 TeV*, Phys. Rev. C **88** (4 2013) 044910, URL: <https://link.aps.org/doi/10.1103/PhysRevC.88.044910> (cit. on p. 7).
- 232